



# Regular $\gamma/\gamma'$ phase interface instability in a binary model nickel-based single-crystal alloy



X. Li<sup>a,\*</sup>, X.N. Zhang<sup>a,\*</sup>, C.P. Liu<sup>a</sup>, C.Y. Wang<sup>b,c</sup>, T. Yu<sup>c</sup>, Z. Zhang<sup>d,\*</sup>

<sup>a</sup> Institute of Microstructure and Property of Advanced Materials, Beijing University of Technology, Beijing 100124, China

<sup>b</sup> Department of Physics, Tsinghua University, Beijing 100084, China

<sup>c</sup> Central Iron & Steel Research Institute, Beijing 100081, China

<sup>d</sup> State Key Laboratory of Silicon Materials, Department of Materials Science and Engineering, Zhejiang University, Hangzhou 310027, China

## ARTICLE INFO

### Article history:

Received 15 July 2014

Received in revised form 15 January 2015

Accepted 19 January 2015

Available online 24 January 2015

### Keywords:

Nickel alloys

Thermal treatment

Interface instability

Strain energy

## ABSTRACT

In this paper, long-term thermal treatment of a binary Ni–Al model nickel-based superalloy was performed at 1000 °C for 50 h, 100 h and 200 h. The evolution of the  $\gamma/\gamma'$  interface was studied. As the treatment time increased, the  $\gamma'$  precipitates coarsened and grew. Regular interface instability was observed that the shape of the  $\gamma/\gamma'$  interface changed from flat to wavy. This interfacial instability was caused by the dynamic balance of strain energy and surface energy at the interface between the two phases. In addition, secondary  $\gamma'$  precipitates were observed after long-term treatment and some of the larger ones took on pillow-like shapes. The pillow-shaped distortion was because that the growth rate of the cube vertices was faster than that of other locations due to the different strain states at different locations.

© 2015 Elsevier B.V. All rights reserved.

## 1. Introduction

Nickel-based single-crystal superalloys, which consist of a high volume fraction of ordered  $L1_2$   $\gamma'$  precipitates coherent with the disordered fcc  $\gamma$  matrix, are widely used in turbine blades and turbine disks because of their excellent creep resistance [1–3]. The creep resistance and deformation behavior of these superalloys are sensitively affected by the morphology and size of  $\gamma'$  precipitates [4–6]. Rafting is a common and important phenomenon during the creep process of nickel-based single crystal superalloys [7,8], during which the morphology and size of the  $\gamma'$  precipitates change. At the same time, the  $\gamma/\gamma'$  phase interface also changes. It is important to study the phase interfacial evolution for understanding the relationship between microstructure and properties. Some researchers investigated the rafting and focused on the morphology change of the  $\gamma'$  phase and the  $\gamma/\gamma'$  interfacial dislocation in the creep process. The  $\gamma/\gamma'$  phase interface evolution and irregular instability has been shown [9–12]. In addition, the  $\gamma/\gamma'$  phase interface irregular instability has also been shown in the long-term thermal treatment process (or thermal exposure in some papers) [13,14], which is a simplified method for investigating the influence of high temperature on the microstructure. However, few

studies specifically talked about this question. As we known, only Prof. Zhu's group discussed the relationship between different types of interfacial protrusions and dislocation motion in the creep process for a DD6 superalloy [15].

In present study, the evolution of the  $\gamma/\gamma'$  phase interface in a model nickel-based single-crystal superalloy was investigated at the atomic scale. Regular interface instability was observed and its mechanism was discussed in detail.

Nickel-based single-crystal superalloys are composed of many elements. These alloying elements affect the property differently depending on the external conditions [16–19]. This complicates evolution of the  $\gamma/\gamma'$  interface, thus a model alloy was selected in present study.

## 2. Experimental

To investigate the intrinsic evolution of the  $\gamma/\gamma'$  phase interface, a binary model alloy with the chemical composition of 82.71% Ni–17.29% Al (at.%) was selected. The ingot was directionally solidified in the  $\langle 001 \rangle$  direction at a constant withdrawal rate of 2 mm/min by the Bridgman technique. The single-crystal ingot was subjected to solid-solution treatment at 1330 °C for 1 h under flowing argon atmosphere, followed by a water quench. Then the alloy was aged at 870 °C for 32 h, also followed by a water quench to room temperature [20].

Slices with the thickness of about 0.4 mm were cut from the single crystal ingot to prepare long-term thermal treatment specimens. The slices were sealed in silica envelopes and thermal treated in a tube furnace at 1000 °C for 50, 100, and 200 h, followed by air quench. For scanning electron microscopy (SEM), the specimens were mechanically polished and electrically etched in a solution of 48%

\* Corresponding authors. Tel.: +86 13718042826 (X.N. Zhang).

E-mail addresses: [xnzhang@bjut.edu.cn](mailto:xnzhang@bjut.edu.cn) (X.N. Zhang), [zezhang@zju.edu.cn](mailto:zezhang@zju.edu.cn) (Z. Zhang).

H<sub>2</sub>SO<sub>4</sub> + 40% HNO<sub>3</sub> + 12% H<sub>3</sub>PO<sub>4</sub>. For transmission electron microscopy (TEM), the specimens were thinned by mechanical abrasion and then electrically polished at 30 V in a solution of 13% perchloric acid and 7% glycerin in acetic acid.

The SEM experiments were operated using Quanta 600F at an accelerating voltage of 20 kV. The TEM experiments were operated using JEM-2010F microscope at an accelerating voltage of 200 kV. The high resolution TEM experiments were also performed using JEM-2010F at an accelerating voltage of 200 kV. The beam was (001) orientation.

### 3. Results and discussion

Fig. 1 shows the microstructure evolution under thermal treatment at 1000 °C for 50, 100, and 200 h. The specimen exhibited a two-phase  $\gamma/\gamma'$  microstructure (Fig. 1(a)) before long-term thermal treatment. The initial primary  $\gamma'$  precipitates were generally cubic with an average size of  $\sim 300$ –500 nm. The  $\gamma'$  precipitates grow up in size with increasing aging time (Fig. 1(b)–(d)). The growth rates in all three dimensions were nearly same. Over time, the initial cubic  $\gamma'$  precipitates connected to each other and gradually coarsened. After 50 h (Fig. 1(b)), the  $\gamma'$  precipitates obviously grew. The average size was  $\sim 2$   $\mu\text{m}$ , and some particles reached 3  $\mu\text{m}$ . After 100 h, the average size grew to  $\sim 3$ –4  $\mu\text{m}$ , as shown in Fig. 1(c). After 200 h, the average size increased further to  $\sim 5$   $\mu\text{m}$  (Fig. 1(d)).

Secondary  $\gamma'$  precipitates were observed after thermal treatment, revealed by the [001]-axis diffraction pattern shown in the inset of Fig. 1(c). The average size of these secondary precipitates was  $\sim 100$  nm. After 50 h, a small amount of these particles were generated. After 100 h, their number obviously increased. After 200 h, a large amount of secondary particles can also be observed, as shown in Fig. 1(d).

It was worth of attention that after long-term thermal treatment, the phase interface between the  $\gamma'$  precipitates and the  $\gamma$  matrix changed from straight to wavy, as shown in the red square in Fig. 2(a). These waves occurred in regular arrays, as shown in Fig. 2(b). The high-resolution electron microscopy image in Fig. 2(c) shows that the  $\gamma/\gamma'$  phase interface was not straight. There were atomic-scale steps oriented in the  $\langle 001 \rangle$  direction. The

high-resolution image was obtained from the wave-peak region, marked by the white square in Fig. 2(b).

Note that some of the larger secondary  $\gamma'$  particles took on pillow-like shapes, while the smaller ones were cubic, as shown by the white frame in Fig. 2(a). The formation of the pillow-like shape was caused by the faster growth rate of the cube vertices.

In nickel-based single-crystal superalloys, the  $\gamma'$  and  $\gamma$  phases remain coherent because their lattice parameters are close. The lattice parameter of the  $\gamma'$  phase is slightly larger than that of the  $\gamma$  matrix for the model alloy in the present study, generating an elastic stress field near the  $\gamma'/\gamma$  interface area. The  $\gamma'$  precipitates and  $\gamma$  matrix are subjected to compressive stress and tensile stress, respectively, as schematically shown in Fig. 3(a).

It has been reported that the interfacial evolution was determined by the balance of strain energy and interface energy [21–24]. The strain energy comes from the lattice misfit of the two phases. The phase interface instability can be explained from this point. By measuring the interplanar spacing from the high-resolution TEM images, the lattice parameters of the two phases can be obtained. The measurement method was schematically shown in Fig. 3(b). Ten sets of interplanar spacings were measured per time at the location away from the interface, then performing measurement three times at different locations. These measurements were averaged to obtain the final results, given in Table 1. The lattice misfit of the two phases was calculated by

$$\delta = \frac{a_{\gamma'} - a_{\gamma}}{a_{\gamma}}, \quad (1)$$

where  $a_{\gamma'}$  and  $a_{\gamma}$  are the lattice diameters of  $\gamma'$  and  $\gamma$ , respectively. The lattice misfit between the two phases increased with thermal treatment time. To keep the phases coherent, the strain energy caused by lattice misfit at the phase interface will increase.

The elastic strain energy can be expressed as [21]

$$W = \int_0^{\varepsilon^e} \sigma_{ij} d\varepsilon_{ij}^e, \quad (2)$$

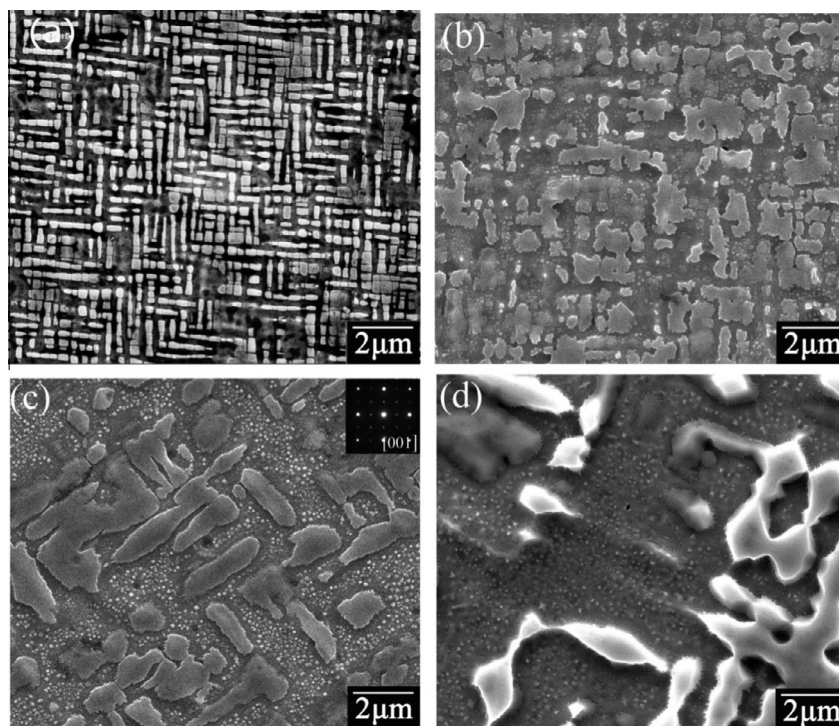
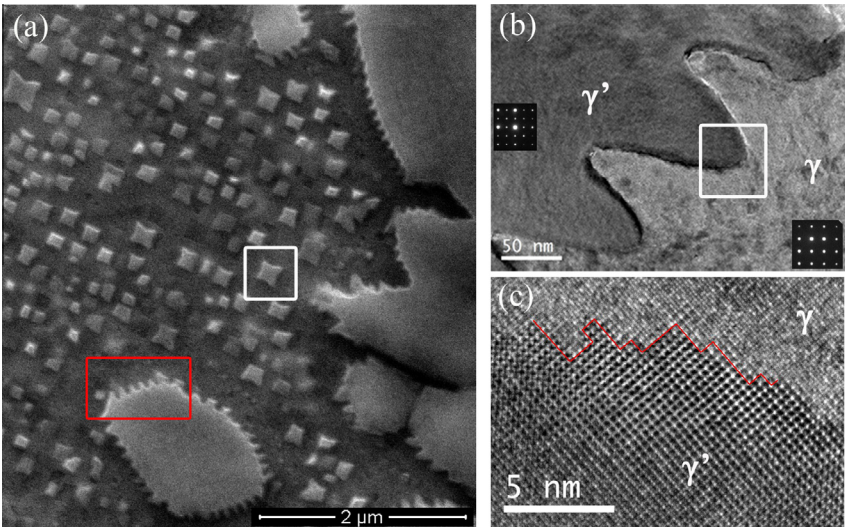
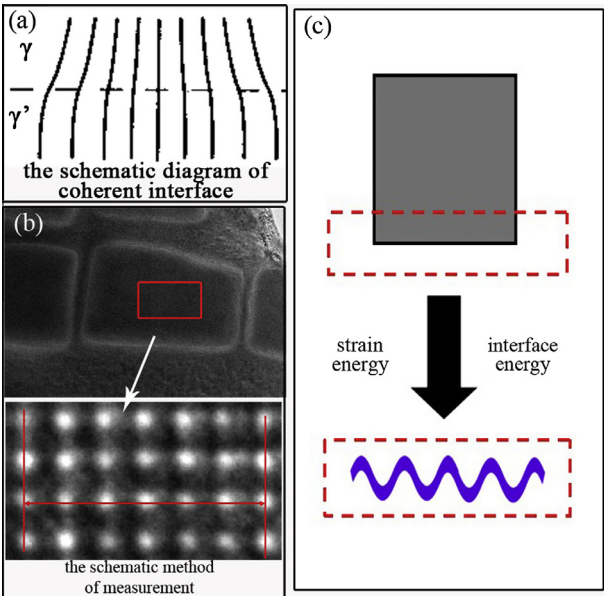


Fig. 1. Microstructure evolution with standard heat treatment (a) and long-term thermal treatment at 1000 °C for 50 h (b), 100 h (c) and 200 h (d).



**Fig. 2.** The microstructure of wavy-like edges of  $\gamma'$  precipitates with long term thermal treatment at 1000 °C for 200 h (a), the enlarged image of the wavy-like shape (b), the small steps along  $\langle 001 \rangle$  direction at the  $\gamma'/\gamma$  interface.



**Fig. 3.** The schematic diagram of coherent interface (a), the schematic measurement of lattice parameter (b) and the schematic model of the interface evolution (c).

where  $\epsilon_{ij}^e$  is the elastic strain tensor and  $\sigma_{ij}$  is the stress. The strain energy caused by lattice misfit between the two phases increases with interface strain. The results in Table 1 show that the lattice misfit between the two phases increased with thermal treatment time, increasing the interface strain and elastic strain energy.

When the strain energy increases beyond a critical value, the interface energy cannot balance it. Increase of interface energy

can release the strain energy, forming a new balance. The interface energy can be described by

$$E = \lambda \cdot s, \tag{3}$$

where  $\lambda$  is the interface energy per unit area and  $s$  is the total area of the interface. Increasing interface area is a valid and common mode to release strain energy. This is why the  $\gamma'/\gamma$  phase interface changed from flat to wavy in the present study. During long-term treatment, the interface strain energy increased with treatment time, to keep balance, the interface energy must increase by increasing the interface area, inducing the interface instability we observed. The schematic model of the interface evolution is given in Fig. 3(c).

The  $\langle 001 \rangle$  elastic strain energy is greater than that in other directions because of the low Young's modulus. Under high elastic strain energy at a coherent interface, the  $\langle 001 \rangle$  direction can contain more strain than other directions. Therefore,  $\gamma'$  precipitates preferentially coarsen and grow along the  $\langle 001 \rangle$  direction [25]. This is consistent with the phenomenon of the small steps along the  $\langle 001 \rangle$  direction in Fig. 2(c).

The strain energy can also be released by forming misfit dislocations at the interface between two phases. As the treatment time increased, the lattice misfit between the  $\gamma'$  precipitates and  $\gamma$  matrix increased. This misfit can be accommodated by the formation of interface dislocations. Some dislocations were observed at the phase interface. The inverse fast Fourier transformation of Fig. 4(a), shown in Fig. 4(b), help show the interface dislocations.

The pillow-shaped distortion of some secondary  $\gamma'$  precipitates was caused by faster growth rate of the cube vertices than that of other locations, in turn caused by the different strain states. The cube vertices have minimal strain, which is favorable for growth [26]. It has been reported that the growth rate of precipitates changes from interactions between the precipitate strain field

**Table 1**  
the lattice misfit between  $\gamma'$  precipitates and  $\gamma$  matrix after long-term thermal treatment.

	$\gamma'$ (–)/nm	Standard deviation	$\gamma$ (–)/nm	Standard deviation	Lattice misfit $\delta = (a_{\gamma'} - a_{\gamma})/a_{\gamma}$
Initial state	0.3501	0.0017	0.3470	0.0019	0.89%
1000 °C, 50 h	0.3560	0.0018	0.3453	0.0018	3.10%
1000 °C, 100 h	0.3608	0.0017	0.3427	0.0018	5.28%
1000 °C, 200 h	0.3628	0.0020	0.3412	0.0019	6.33%



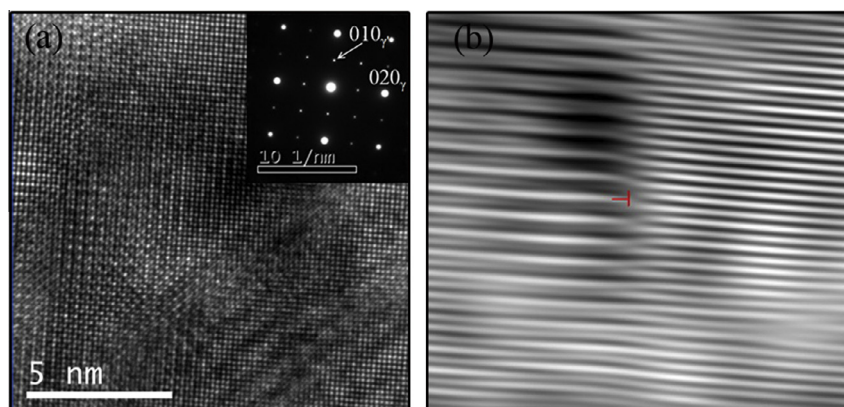


Fig. 4. The high resolution image (a) and the inverse fast Fourier transformation graph under the thermal treatment at 1000 °C for 50 h (b).

and the strain field around the solute atom. If the precipitate strain field is compressive, and if the strain field around the solute atoms is dilatational because the radius of the solute atom is smaller than that of the solvent atom, the interaction energy will be negative, which can provide extra driving force for growth. In contrast, if the interaction energy is positive, the growth will be retarded [27]. In the present study, the strain state around the  $\gamma'$  precipitates was compressive, and the strain field around the solute atom was also compressive because the radius of the Al solute atom was larger than that of the Ni solvent atom. That is, the interaction energy was positive, which decelerated the growth kinetics. Since the strain state of the cube vertices was minimal, the deceleration was minimal. Therefore, the growth rate of the cube vertices was faster than that of other locations. The faster growth rate of the vertices resulted in the pillow-shaped distortion.

#### 4. Conclusions

In summary, we studied the  $\gamma/\gamma'$  phase interface evolution of a binary Ni–Al single-crystal superalloys under long-term thermal treatment at 1000 °C using SEM and TEM. After the long-term thermal treatment, the shape of the  $\gamma/\gamma'$  phase interface changed from straight to wavy, and these waves occurred in regular arrays. The high-resolution electron microscopy image shows that the  $\gamma/\gamma'$  phase interface are not straight at atomic scale, neither. There are atomic-scale steps oriented in the  $\langle 001 \rangle$  direction. The instability of the  $\gamma/\gamma'$  phase interface was explained by assessing the increasing strain energy induced by lattice misfit between the two phases. After thermal treatment, secondary  $\gamma'$  particles formed, and some larger secondary  $\gamma'$  particles grew with pillow-shaped distortion. This distortion was caused by the interactions between the precipitate strain field and the strain field around the solute atoms.

#### Acknowledgements

This work is supported by the National Natural Science Foundation of China (Grant No. 11327901) and the National Basic

Research Program (“973” Project, Ministry of Science and Technology of China, Grant No. 2011CB606402).

#### References

- [1] T.M. Pollock, A.S. Argon, *Acta Metall. Mater.* 40 (1992) 1–30.
- [2] P. Caron, T. Khan, *Aerosp. Sci. Technol.* 3 (1999) 513–523.
- [3] R.C. Reed, *The Superalloys Fundamentals and Applications*, Cambridge University Press, 2006.
- [4] P. Caron, T. Khan, *Mater. Sci. Eng.* 61 (1983) 173–184.
- [5] R.A. MacKay, M.V. Nathal, *Acta Metall. Mater.* 38 (1990) 993–1005.
- [6] T. Murakumo, T. Kobayashi, Y. Koizumi, H. Harada, *Acta Mater.* 52 (2004) 3737–3744.
- [7] N. Matan, D.C. Cox, C.M. Rae, R.C. Reed, *Acta Mater.* 47 (1999) 2031–2045.
- [8] X.F. Yu, S.G. Tian, H.Q. Du, H.C. Yu, M.G. Wang, L.G. Shang, S.S. Cui, *Mater. Sci. Eng., A* 506 (2009) 80–86.
- [9] S.G. Tian, J. Wu, D. Shu, Y. Su, H. Yu, B.J. Qian, *Mater. Sci. Eng., A* 616 (2014) 260–267.
- [10] X.P. Tan, J.L. Liu, T. Jin, Z.Q. Hu, H.U. Hong, B.G. Choi, I.S. Kim, C.Y. Jo, D. Mangelinck, *Mater. Sci. Eng., A* 580 (2013) 21–35.
- [11] L. Agudo Jácome, P. Nörtershäuser, C. Somsen, A. Dlouhý, G. Eggeler, *Acta Mater.* 69 (2014) 246–264.
- [12] L.J. Carroll, Q. Feng, T.M. Pollock, *Metall. Mater. Trans. A* 39 (2008) 1290–1307.
- [13] P.C. Xia, J.J. Yu, X.F. Sun, H.R. Guan, Z.Q. Hua, *J. Alloys Comp.* 443 (2007) 125–131.
- [14] J.L. Liu, T. Jin, J.J. Yu, X.F. Sun, *Mater. Sci. Eng., A* 527 (2010) 890–897.
- [15] M. Huang, Z.Y. Cheng, J.H. Xiong, J.R. Li, J.Q. Hu, Z.L. Liu, J. Zhu, *Acta Mater.* 76 (2014) 294–305.
- [16] A. Sato, H. Harada, T. Yokokawa, T. Murakumo, Y. Koizumi, T. Kobayashi, H. Imai, *Scr. Mater.* 54 (2006) 1679–1684.
- [17] A.C. Yeh, S. Tin, *Scr. Mater.* 52 (2005) 519–524.
- [18] B.H. Ge, Y.S. Luo, J.R. Li, J. Zhu, *Scr. Mater.* 63 (2010) 969–972.
- [19] W.Z. Wang, T. Jin, J.L. Liu, X.F. Sun, H.R. Guan, Z.Q. Hu, *Mater. Sci. Eng., A* 479 (2008) 148–156.
- [20] X.X. Yu, C.Y. Wang, X.N. Zhang, P. Yan, Z. Zhang, *J. Alloys Comp.* 582 (2014) 299–304.
- [21] S. Socrate, D.M. Parks, *Acta Metall. Mater.* 41 (1993) 2185–2209.
- [22] J. Tiley, G.B. Viswanathan, R. Srinivasan, R. Banerjee, D.M. Dimiduk, H.L. Fraser, *Acta Mater.* 57 (2009) 2538–2549.
- [23] J. Coakley, H. Basoalto, D. Dye, *Acta Mater.* 58 (2010) 4019–4028.
- [24] T. Wang, G. Sheng, Z.K. Liu, L.Q. Chen, *Acta Mater.* 56 (2008) 5544–5551.
- [25] L. Muller, U. Glatzel, M. Feller-Kniepmeier, *Acta Metall. Mater.* 40 (1992) 1321–1327.
- [26] R.A. Ricks, A.J. Porter, R.C. Eob, *Acta Metall.* 31 (1983) 43–53.
- [27] R. Sankaran, G. Laird, *Acta Metall.* 22 (1974) 957–969.